

## Article

# Alkali and Alkali-Earth Metals Incorporation to Ni/USY Catalysts for CO<sub>2</sub> Methanation: The Effect of the Metal Nature

M. Carmen Bacariza <sup>1,\*</sup> , Cláudia Grilo <sup>1</sup>, Paula Teixeira <sup>1</sup> , José M. Lopes <sup>1,2</sup>  and Carlos Henriques <sup>1,2</sup> 

<sup>1</sup> Centro de Química Estrutural (CQE), Instituto Superior Técnico, Universidade de Lisboa, Avenida Rovisco Pais, 1049-001 Lisboa, Portugal; claudiafontesgrilo@tecnico.ulisboa.pt (C.G.); paula.teixeira@tecnico.ulisboa.pt (P.T.); jmlopes@tecnico.ulisboa.pt (J.M.L.); carlos.henriques@tecnico.ulisboa.pt (C.H.)

<sup>2</sup> Departamento de Engenharia Química (DEQ), Instituto Superior Técnico, Universidade de Lisboa, Avenida Rovisco Pais, 1049-001 Lisboa, Portugal

\* Correspondence: maria.rey@tecnico.ulisboa.pt

**Abstract:** CO<sub>2</sub> methanation is typically carried out using Ni-supported catalysts containing promoters such as alkali or alkali-earth metals to improve their properties. In this work, bimetallic Ni-based USY zeolite catalysts containing alkali (Li, K and Cs) and alkali-earth (Mg, Ca) metal compounds were prepared using the same conditions (15 wt% of metals; co-impregnation), characterized by N<sub>2</sub> sorption, XRD, TGA, CO<sub>2</sub> adsorption–desorption, DRS UV-Vis and H<sub>2</sub>-TPR, and finally applied in CO<sub>2</sub> methanation reaction (86,100 mL h<sup>-1</sup> g<sup>-1</sup>, P<sub>CO<sub>2</sub></sub> = 0.16 bar, H<sub>2</sub>:CO<sub>2</sub> = 4:1). For each group, the effects of the second metal nature on the properties and performances were assessed. Alkali metals incorporation induced considerably low catalytic performances (CH<sub>4</sub> yields < 26%), attributed to their negative impact on zeolite structure preservation. On the contrary, alkali-earth metal-containing catalysts exhibited lower structural damage. However, the formation of Ni-Mg mixed oxides in Ni-Mg/USY catalyst and CaCO<sub>3</sub> during the reaction in Ni-Ca/USY sample could explain their performances, similar or lower than those obtained for Ni/USY catalyst. Among the studied metals, calcium was identified as the most interesting (CH<sub>4</sub> yield of 65% at 415 °C), which was ascribed to the slight improvement of the Ni<sup>0</sup> dispersion.

**Keywords:** CO<sub>2</sub> methanation; CO<sub>2</sub> adsorption; basic oxides; alkali metals; alkali-earth metals; nickel catalysts; co-impregnation



**Citation:** Bacariza, M.C.; Grilo, C.; Teixeira, P.; Lopes, J.M.; Henriques, C. Alkali and Alkali-Earth Metals Incorporation to Ni/USY Catalysts for CO<sub>2</sub> Methanation: The Effect of the Metal Nature. *Processes* **2021**, *9*, 1846. <https://doi.org/10.3390/pr9101846>

Academic Editors: Paola Ammendola and Vincent Terrasson

Received: 22 July 2021

Accepted: 14 October 2021

Published: 18 October 2021

**Publisher's Note:** MDPI stays neutral with regard to jurisdictional claims in published maps and institutional affiliations.



**Copyright:** © 2021 by the authors. Licensee MDPI, Basel, Switzerland. This article is an open access article distributed under the terms and conditions of the Creative Commons Attribution (CC BY) license (<https://creativecommons.org/licenses/by/4.0/>).

## 1. Introduction

CO<sub>2</sub> methanation, an important reaction in the current context of renewable energies expansion [1,2], is typically carried out using metal-supported catalysts [3–10]. Among all, Ni/Al<sub>2</sub>O<sub>3</sub> catalysts are the most widely studied, as they lead to high activity and selectivity to methane and, unlike noble metals, have a more favorable cost-efficiency ratio. Despite being one of the most used metals, the utilization of nickel as active metal still requires solutions to some problems such as sintering, reoxidation, carbon deposition and sulfur poisoning [11]. In this way, the nature and properties of the chosen support can influence the metallic dispersion, the electronic properties and also play an important role in the activation of CO<sub>2</sub> and, consequently, in their catalytic performance and stability. In this context, other types of supports such as CeO<sub>2</sub>, ZrO<sub>2</sub>, SiO<sub>2</sub>, carbons, hydrotalcites, metal organic frameworks or zeolites have revealed promising results in the literature [3–10]. Furthermore, the incorporation of rare-earth metal oxides (e.g., CeO<sub>2</sub>, La<sub>2</sub>O<sub>3</sub>, Y<sub>2</sub>O<sub>3</sub>) is a common strategy to improve the properties of Ni catalysts. However, their high cost and limited availability requires the identification of alternative promoters.

Among the studied supports, zeolites have been identified as suitable due to their easily tunable properties in terms of metal-support interactions, metallic dispersion, hydrophobicity or basicity [12]. Most of the reported studies on zeolites application in carbon

dioxide methanation reaction have been carried out using Ni as active metal and rare-earth metal oxides as promoters [10,12]. However, as already pointed out, the identification of alternative additives based on more abundant and/or inexpensive metals is mandatory.

One potential strategy toward the synthesis of cost-efficient catalysts for CO<sub>2</sub> methanation is the use of alkali and alkali-earth metal compounds as promoters. Their potential incorporation in CO<sub>2</sub> methanation catalysts formulation was reported for systems containing Ni, Co or Ru as active metals and Al<sub>2</sub>O<sub>3</sub>, SiO<sub>2</sub>, CeO<sub>2</sub> or TiO<sub>2</sub> as supports [13–20], and summarized in a complete review elaborated by Tsiotsias et al. [21]. Overall, and besides the cost and abundancy issues, the main benefits derived from the incorporation of alkali and alkali-earth metals arise from the improvement of the CO<sub>2</sub> adsorption capacity and the modification of the active metal properties (e.g., metal-support interactions, metallic dispersion, electronic properties) [21]. These compounds were reported as able to strengthen the interaction between the active metal particles and the support, hindering the occurrence of sintering processes and improving the metallic dispersion [21]. Additionally, their incorporation over metal-supported CO<sub>2</sub> methanation catalysts could result in the creation of new active sites for carbon dioxide adsorption, affecting the mechanistic steps [21].

However, despite the potential of incorporating different alkali and alkali-earth metals to CO<sub>2</sub> methanation catalysts, no systematic studies have discussed this topic in Ni/Zeolites thus far. Consequently, the present work aimed at the synthesis, characterization and catalytic testing of Ni catalysts containing alkali (Li, K and Cs) or alkali-earth (Mg and Ca) oxides supported on a previously optimized zeolite [22,23]. By keeping the same preparation conditions and metal loadings, a screening study based on the influence of the alkali/alkali-earth metal nature on the catalysts' properties and performances toward CO<sub>2</sub> methanation was performed. The alkali/alkali-earth metals loading was chosen considering that, in the literature for Ni-based zeolites applied in CO<sub>2</sub> methanation [10,12], where only La, Ce and Mg were reported as promoters, the loadings chosen for these metals were up to 20 wt%. In addition to this, the use of alkali/alkali-earth metals loadings above 10 wt% in catalysts supported over other types of materials (e.g., Al<sub>2</sub>O<sub>3</sub>, SiO<sub>2</sub>, ZrO<sub>2</sub>) was reported [21]. Consequently, as a starting point for studying the addition of these metals to Ni-based zeolites and in order to compare with other promoters already reported in literature for this type of catalysts, 15 wt% of alkali/alkali-earth metals and 15 wt% of Ni were used. Samples were prepared by co-impregnation method and characterized by N<sub>2</sub> sorption, powder X-ray diffraction (XRD), thermogravimetric analysis (TGA), CO<sub>2</sub> adsorption–desorption cycles by TGA, diffuse reflectance spectroscopy UV-Vis (DRS UV-Vis) and H<sub>2</sub> temperature programmed reduction (H<sub>2</sub>-TPR). Finally, they were catalytically tested under CO<sub>2</sub> methanation conditions.

## 2. Materials and Methods

### 2.1. Catalysts Preparation

In this work, a commercial ultrastable Y zeolite (CBV 780, <0.02 wt% Na) provided by Zeolyst with a global Si/Al ratio of  $\approx 38$  and without extra-framework aluminum (EFAL) species was used as starting material. Based on previous findings [22,23], this zeolite was ion-exchanged with Cs<sup>+</sup> to improve its hydrophobicity and CO<sub>2</sub> affinity, being the final material (named as USY) used as support for all catalysts from the present work. First, a monometallic catalyst containing 15 wt% Ni (labeled as Ni/USY) was prepared by incipient wetness impregnation followed by drying (oven, 80 °C and 12 h) and calcination (60 mL min<sup>-1</sup> g<sup>-1</sup> air, 500 °C and 6 h), following a procedure described elsewhere [22,24]. The Ni loading was optimized in previous studies. Second, a series of bimetallic catalysts with 15 wt% (nominal value) Ni and containing 15 wt% (nominal value) of alkali (A; Li, K and Cs) and alkali-earth (AE; Mg and Ca) metals (labeled as Ni-(A or AE)/USY) were synthesized by co-impregnation followed by drying (oven, 80 °C and 12 h) and calcination (60 mL min<sup>-1</sup> g<sup>-1</sup> air, 500 °C and 6 h), using the protocol reported in our former studies [25]. Finally, in order to confirm the positive effect of using 2-propanol (2-PrOH) as impregnation solvent in the Ni<sup>0</sup> dispersion [26], the best bimetallic catalyst was again prepared using

2-PrOH. Further information regarding reagents purity and supplier can be found in the Supplementary Materials.

## 2.2. Characterization Techniques

Catalysts were characterized as described in previous studies [25]. Overall, N<sub>2</sub> sorption was carried out on an Autosorb iQ equipment from Quantachrome, being micropores volumes ( $V_{\text{micro}}$ ) and external surface areas ( $S_{\text{ext}}$ ) obtained from *t*-plot using de Boer method, total pore volumes ( $V_{\text{total}}$ ) measured at a relative pressure ( $p/p^0$ ) of 0.95 and mesopores volumes ( $V_{\text{meso}}$ ) determined as  $V_{\text{total}} - V_{\text{micro}}$ . Powder XRD patterns were collected using a Bruker AXS Advance D8 diffractometer equipped with a 1D detector (SSD 160) and using a Ni filter. The scanning range was set from 5 to 80° (2θ), with a step size of 0.03° and a step time of 0.5 s. The analysis of the obtained patterns was performed using EVA software (Bruker), identifying the match between the experimental pattern and the Crystallography Open Database (COD). NiO/Ni<sup>0</sup> crystallite sizes were determined using Scherrer equation and metallic dispersion was estimated using Ni<sup>0</sup> crystallite sizes as described elsewhere [27]. TGA was conducted for catalysts saturated with water vapor using a Setsys Evolution equipment from Setaram instruments, being hydrophobic indexes (h) determined as the ratio between the mass losses at 150 and 400 °C. DRS UV-Vis spectra were collected using a Varian Cary 5000 UV-Vis-NIR spectrophotometer equipped with a diffuse reflectance accessory. NiO band gaps were determined as described elsewhere [28–30]. Finally, H<sub>2</sub>-TPR profiles were obtained in an AutoChem II equipment from Micromeritics from room temperature to 900 °C under a 5% H<sub>2</sub>/Ar flow.

In addition, catalysts' CO<sub>2</sub> adsorption capacity was assessed in the same TGA equipment during six adsorption–desorption cycles. First, catalysts' surface were cleaned at 470 °C under N<sub>2</sub> flow. Afterward, CO<sub>2</sub> sorption was carried out at 150 °C (60 min, 25/75 of CO<sub>2</sub>/N<sub>2</sub> flow) and the desorption was performed at 450 °C (10 min, N<sub>2</sub> flow). TGA mass variations registered during the sorption and desorption steps were related to CO<sub>2</sub> adsorption/release along the cycles. The adsorbed CO<sub>2</sub> was estimated using Equation (1), where *m* and *M* are respectively the mass (kg) and the molecular weight (kg/mmol).

$$\text{CO}_{2\text{adsorbed}} = \frac{m_{\text{CO}_2}}{M_{\text{CO}_2} \cdot m_{\text{catalyst}}} \quad (1)$$

## 2.3. Catalytic Tests

Catalytic performances were assessed, as in previous works [25], from 200 to 450 °C (increasing the temperature by steps of ≈25 °C) at 1 bar using a fixed-bed reactor (internal diameter: 17 mm, length: 750 mm) presenting a porous glass filter (P3, pore size between 16 and 40 μm, European porosity designation), where 0.200 g of catalyst in powder form (particle size < 63 μm) were loaded. Pressure drop during the experiment was measured with a manometer and a leak detector equipment (Inficon GAS-Mate GAS-Mate Combustible Gas Leak Detector) was used to guarantee the absence of leaks in the system during the experiments.

An in situ pre-reduction step was first performed (470 °C, 2.5 °C min<sup>−1</sup>, molar ratio of H<sub>2</sub>:N<sub>2</sub> = 4:1, total flow of 250 mL min<sup>−1</sup>), being the used temperature previously optimized [22,31]. In the case of Ni-Mg/USY catalyst, an additional test was performed after a pre-reduction step at 740 °C. For the reaction, a mixture of H<sub>2</sub>, CO<sub>2</sub> and N<sub>2</sub> (inert) was used (molar ratio of H<sub>2</sub>:CO<sub>2</sub>:N<sub>2</sub> = 36:9:10, total flow of 287 mL min<sup>−1</sup>). The reactor effluent was analyzed using Guardian<sup>®</sup> NG infrared detectors (Edinburgh Sensors) for CO<sub>2</sub>, CH<sub>4</sub> and CO and outlet flows were measured for each temperature after reaching the steady state, since this reaction proceeds with a reduction in the number of mol. The corresponding CO<sub>2</sub>, CH<sub>4</sub> and CO molar flows ( $F_{\text{CO}_2,\text{outlet}}$ ,  $F_{\text{CH}_4,\text{outlet}}$  and  $F_{\text{CO},\text{outlet}}$ ) were determined, being CO<sub>2</sub> conversions, CH<sub>4</sub> selectivity and CH<sub>4</sub> yields determined for each reaction temperature using Equations (2)–(4), respectively. Carbon balances confirmed that

CO and CH<sub>4</sub> were the only C-containing products. The experimental relative error was estimated as 2%.

$$\text{CO}_2 \text{ conversion (\%)} = \frac{F_{\text{CO}_2, \text{inlet}} - F_{\text{CO}_2, \text{outlet}}}{F_{\text{CO}_2, \text{inlet}}} \cdot 100 \quad (2)$$

$$\text{CH}_4 \text{ selectivity (\%)} = \frac{F_{\text{CH}_4, \text{outlet}}}{F_{\text{CO}_2, \text{inlet}} - F_{\text{CO}_2, \text{outlet}}} \cdot 100 \quad (3)$$

$$\text{CH}_4 \text{ yield (\%)} = \frac{F_{\text{CH}_4, \text{outlet}}}{F_{\text{CO}_2, \text{inlet}}} \cdot 100 \quad (4)$$

### 3. Results

#### 3.1. Ni-A/USY Catalysts

In this first section, bimetallic catalysts containing alkali metal species were analyzed with the aim of studying the influence of the metal nature on their properties and performances.

##### 3.1.1. Calcined Catalysts Characterization

Samples were first characterized by N<sub>2</sub> sorption for assessing their textural properties, being the isotherms presented in Figure S1 and the V<sub>micro</sub>, V<sub>meso</sub> and S<sub>ext</sub> values exhibited in Table 1. As observed, the incorporation of Ni over the zeolite support led to a reduction of 28–41% in the textural properties (V<sub>micro</sub>, V<sub>meso</sub> and S<sub>ext</sub>), which could be due to the location of NiO particles on the external surface and mesoporous cavities of the material [32]. However, the incorporation of alkali metals together with Ni led to non-porous materials isotherms (type III) with a drastic reduction of the V<sub>micro</sub>, V<sub>meso</sub> and S<sub>ext</sub>, suggesting the damage and/or collapse of the zeolite structure [22,23].

**Table 1.** Main properties obtained for the Ni-A/USY catalysts, Ni/USY reference sample and USY support after calcination.

Catalyst	V <sub>micro</sub> <sup>1</sup> (cm <sup>3</sup> g <sup>-1</sup> )	V <sub>meso</sub> <sup>2</sup> (cm <sup>3</sup> g <sup>-1</sup> )	S <sub>ext</sub> <sup>1</sup> (m <sup>2</sup> g <sup>-1</sup> )	d <sub>NiO</sub> <sup>3</sup> (nm)	h Index <sup>4</sup>	BG <sub>NiO</sub> <sup>5</sup> (eV)
USY	0.25	0.28	282	-	0.94	-
Ni/USY	0.16	0.20	165	20	0.95	3.79
Ni-Li/USY	<0.01	0.04	22	22	0.75	3.60
Ni-K/USY	<0.01	0.02	21	29	0.75	3.59
Ni-Cs/USY	<0.01	0.07	39	21	0.80	3.78

<sup>1</sup> Micropores volume and external surface area obtained from *t*-plot method; <sup>2</sup> mesopores volume obtained as V<sub>total</sub> - V<sub>micro</sub>; <sup>3</sup> average NiO crystallite sized determined applying Scherrer equation; <sup>4</sup> hydrophobicity index obtained from TGA analysis of the catalysts saturated with water; <sup>5</sup> NiO band gap determined using DRS UV-Vis data.

XRD patterns of the calcined samples can be found in Figure 1. The characteristic peaks of the zeolite (faujasite) were found in Ni/USY pattern at 2θ = 5–35° [33]. However, these peaks were not identified in Ni-A/USY catalyst patterns, confirming the severe damage of the zeolite structure suggested by N<sub>2</sub> sorption results. In the case of Ni-Li/USY, the characteristic peaks of Li<sub>2</sub>SiO<sub>3</sub> (19.0, 27.0, 33.2, 38.6, 51.7, 55.6, 59.2, 69.6 and 72.9°) were observed, indicating the reaction of Li with the Si from the support and the consequent collapse of the structure of the zeolite. The synthesis of lithium silicate using mesoporous silicas and/or zeolites was already reported in literature for application in CO<sub>2</sub> capture [34]. In addition to this, diffraction peaks at 21.4, 25.0, 30.5, 31.9 and 37.5° could be ascribed to LiOH·H<sub>2</sub>O, evidencing the presence of this compound in the calcined catalyst. Based on literature [35], the formation of Li<sub>4</sub>SiO<sub>4</sub> during the calcination treatment is expected. However, after contacting with the ambient, its conversion into Li<sub>2</sub>SiO<sub>3</sub> and Li<sub>2</sub>O (followed by hydroxylation forming LiOH·H<sub>2</sub>O) was reported [35], which could explain the presence of these species in Ni-Li/USY sample.

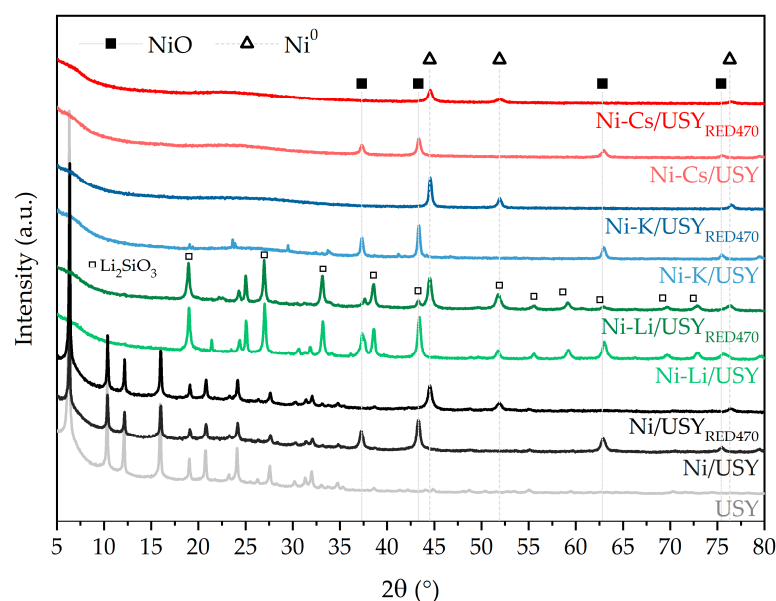


**Figure 1.** XRD patterns obtained for Ni-A/USY catalysts after calcination and reduction.

In the case of Ni-K/USY and Ni-Cs/USY catalysts, no clear diffraction peaks attributed to K or Cs oxides/hydroxides could be identified. However, the presence of these species in the samples was expected, being the absence of intense diffraction peaks related to their high dispersion (average crystallite sizes below the detection limit,  $\approx 5$  nm) or the formation of amorphous glass structures. Furthermore, NiO diffraction peaks were observed in calcined samples ( $37.3$ ,  $43.3$ ,  $62.8$  and  $75.4^\circ$ ), being the average crystallite sizes (Table 1) not improved by the incorporation of alkali metals. Among them, K was responsible for an important increase in the NiO crystallites size (29 nm) when compared to the monometallic Ni/USY reference (20 nm).

Furthermore, and considering the inhibitory role of water in this reaction [12,36], the hydrophobic properties of the catalysts were assessed by TGA (mass loss and heat flow profiles presented in Figure S2). As observed in Figure S2, while in the case of Ni/USY and Ni-Cs/USY a main mass loss process occurred at 107 and 102  $^\circ\text{C}$ , respectively, catalysts containing Li and K exhibited different behaviors. In the case of Ni-Li/USY, a first mass loss step occurred at 87  $^\circ\text{C}$ , followed by a second process close to 300  $^\circ\text{C}$ , in agreement with literature results obtained for  $\text{LiOH}\cdot\text{H}_2\text{O}/\text{NaY}$  zeolite [37]. In the case of Ni-K/USY, two processes were identified at 94 and 143  $^\circ\text{C}$ . This indicates the presence of water interacting with different strengths with the materials (e.g., adsorbed or structural water). The  $h$  indexes presented in Table 1 indicate that the high hydrophobic character of USY and Ni/USY (indexes  $\approx 1$ ) was reduced with the incorporation of alkali metals in the formulation. As the hydrophobicity of this material is related with the high Si/Al ratio of the structure as well as the presence of large compensating cations, the severe damage suffered could contribute to this behavior. In addition, for Ni-Li/USY catalyst, the high hydrophilicity of  $\text{LiOH}\cdot\text{H}_2\text{O}$  was already reported [37]. Overall, Ni-Cs/USY catalyst presented the highest hydrophobicity among the bimetallic Ni-A/USY samples.

In addition, the interaction of catalysts with carbon dioxide was analyzed by performing  $\text{CO}_2$  adsorption–desorption cycles, typically used for assessing sorbents' ability to capture  $\text{CO}_2$ . As observed in Figure 2, where catalysts'  $\text{CO}_2$  adsorption capacity is presented along the cycles, Ni-Li/USY exhibited the highest ability to adsorb  $\text{CO}_2$ , followed by Ni-Cs/USY, Ni/USY and, finally, Ni-K/USY, which displayed negligible results. The highest capacity of Ni-Li/USY could be related with lithium silicate ability to capture  $\text{CO}_2$ , as reported in literature [34,38]. In addition, all catalysts presented a decrease in the  $\text{CO}_2$  adsorption capacity over the cycles, i.e., 30, 34 and 36% for Ni/USY, Ni-Cs/USY and Ni-Li/USY, respectively ( $(\text{CO}_2\text{ sorption } 1\text{cy} - \text{CO}_2\text{ sorption } 6\text{cy}) / \text{CO}_2\text{ sorption } 1\text{cy} \cdot 100$ ). This loss may be due to the formation of stable nickel, lithium or cesium carbonates, whose de-

composition occurs at temperatures above 700 °C [39,40], reducing the number of available CO<sub>2</sub> adsorption sites. To avoid catalysts' damage and mimic the methanation temperature conditions, the desorption step was performed at 450 °C.

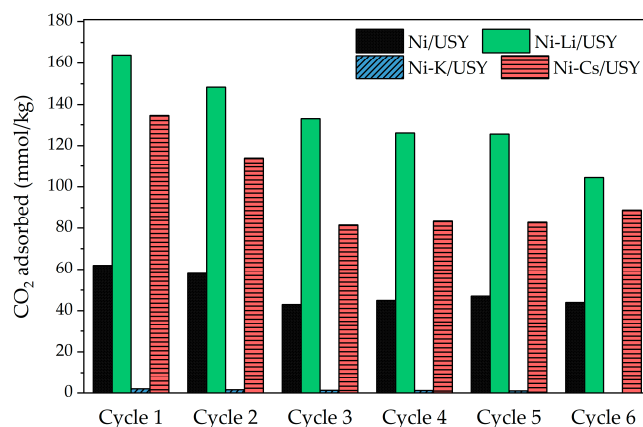


**Figure 2.** CO<sub>2</sub> adsorption capacity of Ni/USY and Ni-A/USY catalysts under cyclic experiments. Adsorption was performed at 150 °C (CO<sub>2</sub>/N<sub>2</sub>; 60 min) and desorption at 450 °C (N<sub>2</sub>; 10 min).

Furthermore, catalysts were characterized by DRS UV-Vis, being the collected spectra presented in Figure S3 and the calculated NiO band gaps in Table 1. As seen in Figure S3, NiO characteristic bands can be found at  $\approx 290$ ,  $\approx 430$  and  $\approx 725$  nm. In addition, a shift on the first band toward higher wavelengths (redshift) can be observed for Ni-Li/USY and, specially, for Ni-K/USY. This displacement may be associated with the presence of aggregated NiO particles in these samples [41–43], which is in agreement with the crystallite sizes presented in Table 1. In addition to this, NiO band gaps were determined, as they can be indicators of the electronic properties of the catalysts as well as the degree of metals agglomeration. Li- and K-containing catalysts presented lower values, which may be due to the presence of larger NiO particles on these samples.

In terms of reducibility, characterized by the collection of H<sub>2</sub>-TPR profiles (Figure 3), the nature of the incorporated alkali metal significantly influenced NiO redox properties. In the profile of Ni/USY, the reduction of NiO located on the external surface of the zeolite ( $\approx 350$  °C) and inside USY mesoporous cavities ( $>500$  °C) could be observed [22]. Regarding the bimetallic samples, the reducibility below 470 °C followed the order: Ni-K/USY > Ni-Cs/USY > Ni-Li/USY. As seen, K incorporation strongly weakened the interaction between NiO and the support, with most of the nickel oxides species reduction occurring below 500 °C, with this behavior confirmed in the literature [13].

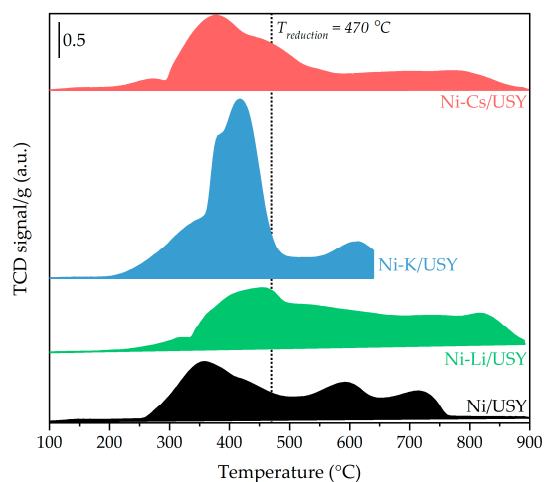


**Figure 3.** H<sub>2</sub>-TPR profiles obtained for Ni-A/USY catalysts. Note that for Ni-K/USY, the experiment was carried till 650 °C to prevent the eventual reaction of K compounds with the quartz reactor.

### 3.1.2. Reduced Catalysts Characterization

Reduced catalysts were characterized by XRD, and the results are exhibited in Figure 1. In agreement with the results for calcined catalysts, no peaks ascribed to the USY zeolite support were found in the bimetallic samples, while the presence of Ni<sup>0</sup> phases was identified in all cases at 44.5, 51.9 and 76.3° (note that peaks found at 43.3 and 62.9° in Ni-Li/USY pattern are ascribed to Li<sub>2</sub>SiO<sub>3</sub> phases and not to NiO). The average Ni<sup>0</sup> crystallite sizes varied as follows: Ni-Cs/USY ( $d_{\text{Ni}^0}$  = 17 nm; dispersion = 5.9%) < Ni/USY ( $d_{\text{Ni}^0}$  = 18 nm; dispersion = 5.6%) < Ni-Li/USY ( $d_{\text{Ni}^0}$  = 19 nm; dispersion = 5.3%) << Ni-K/USY ( $d_{\text{Ni}^0}$  = 26 nm; dispersion = 3.9%). This indicated that, as found for the NiO crystallite sizes (Table 1), the incorporation of alkali metals did not significantly improve catalysts' dispersion, being Ni-K/USY the sample presenting the less dispersed metallic phases. Li<sub>2</sub>SiO<sub>3</sub> diffraction peaks were found on reduced Ni-Li/USY, while K and Cs compounds were not clearly identified in Ni-K/USY and Ni-Cs/USY samples, respectively, in accordance with calcined samples results.

### 3.1.3. Catalytic Performances

Ni-A/USY catalysts were finally tested under CO<sub>2</sub> methanation conditions, being the CO<sub>2</sub> conversion, CH<sub>4</sub> selectivity and CH<sub>4</sub> yields are presented in Figure 4 as a function of the reaction temperature. As observed, bimetallic samples did not reveal higher performances than the Ni/USY reference. CO<sub>2</sub> conversions were lower than 50% in all the range of studied temperatures, varying as follows: Ni-Cs/USY > Ni-Li/USY > Ni-K/USY. In the case of the CH<sub>4</sub> selectivity, always lower than 55%, different trends were observed depending on the alkali metal nature. While for Ni-Li/USY and, specially, Ni-Cs/USY the selectivity to CH<sub>4</sub> increased with the reaction temperature, Ni-K/USY sample presented the highest selectivity to methane at 300 °C (≈30%), decreasing then for 350 °C (≈19%) and stabilizing at ≈24% for 400–450 °C. Consequently, the CH<sub>4</sub> yields, with values <26% in all cases, were similar for Ni-Cs/USY and Ni-Li/USY, being Ni-K/USY the sample leading to the lowest performance (<10% in all the temperature range).

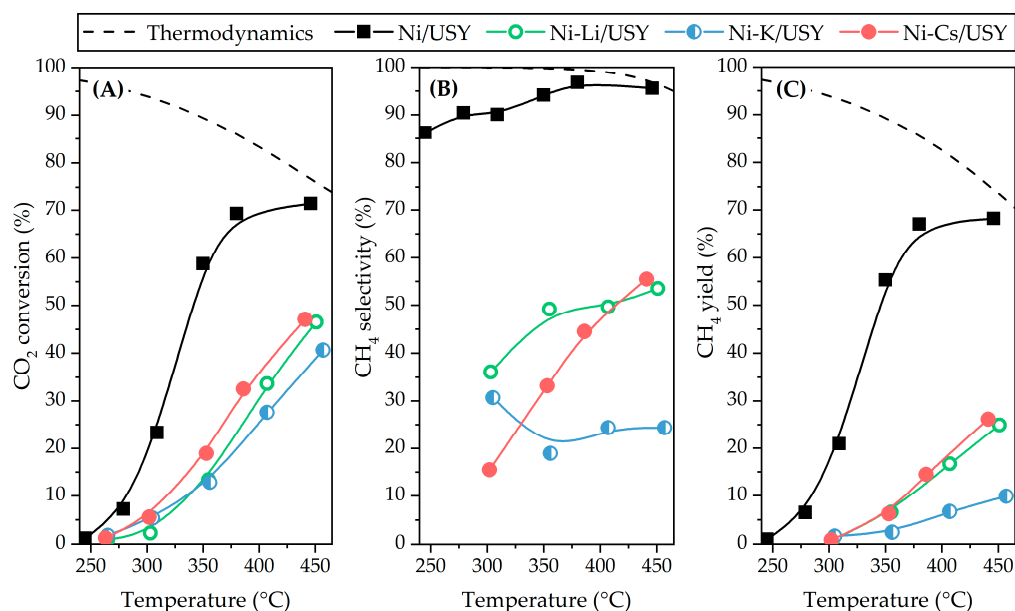


**Figure 4.** Catalytic performances obtained for Ni-A/USY catalysts after reduction at 470 °C: (A) CO<sub>2</sub> conversion; (B) CH<sub>4</sub> selectivity and (C) CH<sub>4</sub> yield. Operating conditions: 1 bar, 86 100 mL h<sup>-1</sup> g<sub>cat</sub><sup>-1</sup> and CO<sub>2</sub>:H<sub>2</sub>:N<sub>2</sub> = 9:36:10.

### 3.1.4. Spent Catalysts Characterization

After catalytic tests, samples were analyzed by XRD, being the corresponding patterns presented in Figure S4. As observed, only Ni<sup>0</sup> phases peaks could be found in the Ni-

K/USY and Ni-Cs/USY spent samples, while lithium silicate and lithium hydroxide were still present in spent Ni-Li/USY, indicating a high stability of these phases. As previously performed, Ni<sup>0</sup> average crystallite sizes were determined applying Scherrer equation, being the obtained values compared to those from reduced samples in Figure S5. Overall, the results suggest the occurrence of sintering or agglomeration of metal particles in the case of Ni-Li/USY catalyst ( $\Delta d_{\text{Ni}^0} = 4 \text{ nm}$ ).

### 3.2. Ni-AE/USY Catalysts

In this second section, bimetallic catalysts containing alkali-earth metal species were analyzed in terms of properties and catalytic performances.

#### 3.2.1. Calcined Catalysts Characterization

Starting by N<sub>2</sub> sorption results (isotherms presented in Figure S6 and textural properties in Table 2), a reduction of the V<sub>micro</sub>, V<sub>meso</sub> and S<sub>ext</sub> was observed in bimetallic samples. Ni-Mg/USY catalyst presented the lowest reduction of the V<sub>micro</sub> and S<sub>ext</sub>, suggesting the preservation of the zeolite structure and/or a higher dispersion of the metal species in this catalyst. In addition, the V<sub>meso</sub> was similar for both Mg and Ca-containing samples.

**Table 2.** Main properties obtained for the Ni-AE/USY catalysts, Ni/USY reference sample and USY support after calcination.

Catalyst	V <sub>micro</sub> <sup>1</sup> (cm <sup>3</sup> g <sup>-1</sup> )	V <sub>meso</sub> <sup>2</sup> (cm <sup>3</sup> g <sup>-1</sup> )	S <sub>ext</sub> <sup>1</sup> (m <sup>2</sup> g <sup>-1</sup> )	d <sub>NiO</sub> <sup>3</sup> (nm)	h Index <sup>4</sup>	BG <sub>NiO</sub> <sup>5</sup> (eV)
USY	0.25	0.28	282	-	0.94	-
Ni/USY	0.16	0.20	165	20	0.95	3.79
Ni-Mg/USY	0.10	0.10	145	-	0.55	-
Ni-Ca/USY	<0.01	0.11	77	18	0.70	3.75

<sup>1</sup> Micropores volume and external surface area obtained from *t*-plot method; <sup>2</sup> mesopores volume obtained as V<sub>total</sub>-V<sub>micro</sub>; <sup>3</sup> average NiO crystallite sized determined applying Scherrer equation; <sup>4</sup> hydrophobicity index obtained from TGA analysis of the catalysts saturated with water; <sup>5</sup> NiO band gap determined using DRS UV-Vis data.

Regarding the structural properties obtained by XRD analysis for calcined samples (Figure 5), the diffraction peaks attributed to the zeolite [33] were observed, which suggested that the drastic reduction of the V<sub>micro</sub> in the Ni-Ca/USY could not be attributed to the structure collapse but probably to a partial blockage of the pores due to the location of metal species in the entry of these cavities. In addition to this, the presence of CaCO<sub>3</sub> (diffraction peak at 29.4°) could be suggested in Ni-Ca/USY catalyst, being this a result of the contact of the catalyst with the ambient and the easy formation of this compound. Finally, the presence of NiO phases was found in Ni-Ca/USY (average crystallite size of 18 nm—Table 2), while the formation of a solid solution (Ni<sub>x</sub>Mg<sub>(1-x)</sub>O<sub>2</sub>) between Ni and Mg was expected in the case of Ni-Mg/USY (e.g., slight shift of the NiO diffraction peak at ≈43° toward lower values [44,45]), in agreement with previous results obtained for Mg/Ni/USY catalysts in literature [46]. Consequently, it was not possible to determine the average crystallite size of NiO on Ni-Mg/USY, as performed previously for the bimetallic catalysts of this work.

In terms of interaction with water, the determined h indexes (Table 2) suggested that Ni-Mg/USY and Ni-Ca/USY catalysts interacted strongly than Ni/USY with water. In terms of interaction with CO<sub>2</sub>, results from adsorption–desorption cycles are exhibited in Figure 6. As observed, higher CO<sub>2</sub> adsorption capacities were obtained for Ni-Mg/USY, but the Ni-Ca/USY catalyst evidenced a higher stability along the cycles (loss of adsorption capacity ≈ 27%, considerably lower than the ≈50% loss found for Ni-Mg/USY). As previously suggested for Ni-A/USY catalysts, the deactivation of the Ni-Ca/USY sample the adsorption–desorption cycles could be ascribed to the formation of stable calcium carbonate. However, considering the characteristics of Ca-looping process used for CO<sub>2</sub> capture [47,48], the formation of CaCO<sub>3</sub> will be unexpected and/or slow at the adsorption

temperature used (150 °C). In addition, Mg and Ca-containing catalysts exhibited higher CO<sub>2</sub> adsorption capacities than the Ni/USY reference for all cycles.

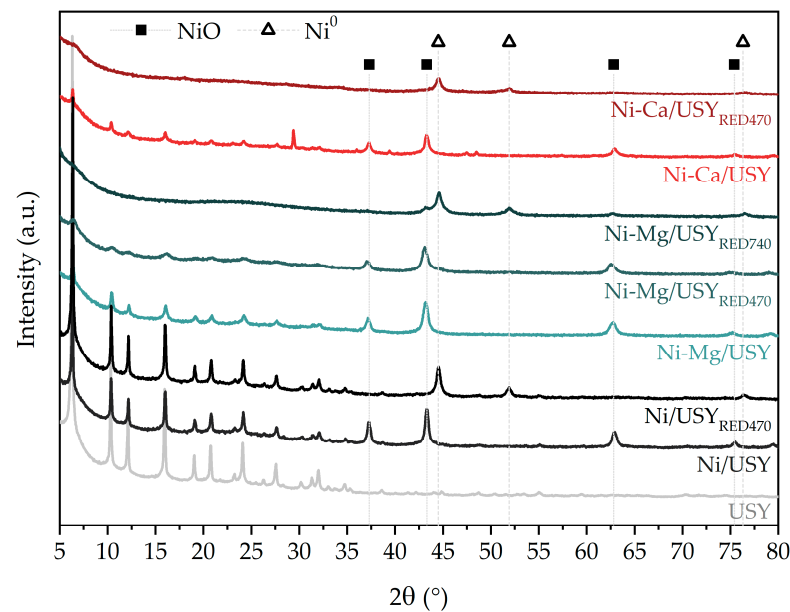


**Figure 5.** XRD patterns obtained for Ni-AE/USY catalysts after calcination and reduction.

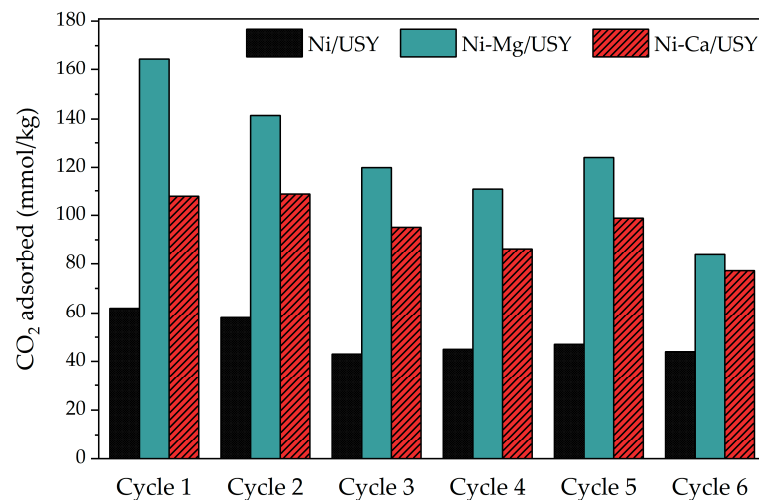


**Figure 6.** CO<sub>2</sub> adsorption capacity of Ni/USY and Ni-AE/USY catalysts under cyclic experiments. Adsorption was performed at 150 °C (CO<sub>2</sub>/N<sub>2</sub>; 60 min) and desorption at 450 °C (N<sub>2</sub>; 10 min).

DRS UV-Vis spectra collected for Ni-AE/USY catalysts can be found in Figure S7, being the profiles similar for both Ni/USY and Ni-Ca/USY. In the case of Ni-Mg/USY catalyst, a shift on the band at  $\approx 290$  nm attributed to NiO was found toward higher wavelengths, but this behavior could not be ascribed to differences in terms of metal aggregation/agglomeration, as in this sample, NiO was not present as a unique phase but in a mixed oxide containing Mg. The NiO band gap determined for the Ni-Ca/USY sample was slightly lower than the obtained for Ni/USY, which was in agreement with the differences in the NiO average crystallite sizes (e.g., larger particles lead to lower band gaps).

Furthermore, H<sub>2</sub>-TPR profiles are presented in Figure 7. In agreement with the literature [46,49], the formation of the Ni-Mg solid solution was confirmed as their typical reduction processes were found above 600 °C, while the presence of free NiO over the zeolite support was expected to be negligible (e.g., no significant reduction processes

occurring below 500 °C). The reduction of surface NiO with a medium interaction with MgO was reported to occur at  $\approx 600$  °C while peaks at  $\approx 700$  °C and  $\approx 800$  °C were attributed to the reduction of NiO on the outermost layer of the  $\text{Ni}_x\text{Mg}_{(1-x)}\text{O}_2$  solid solution [46,49]. Regarding Ni-Ca/USY catalyst, which exhibited a higher reducibility, a profile similar to that of Ni/USY was obtained.

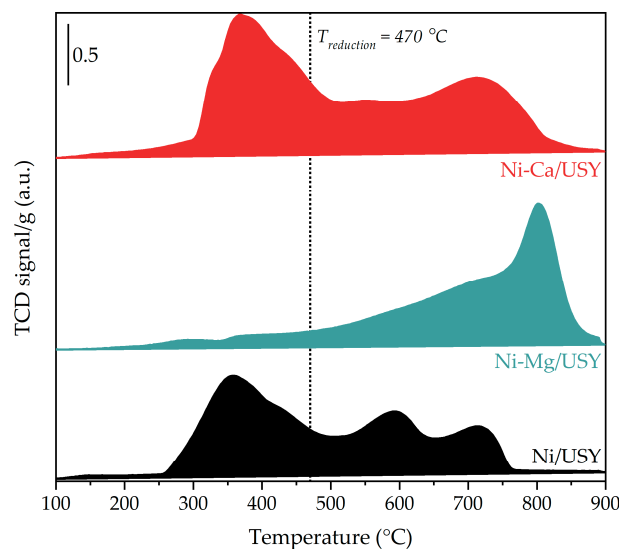


**Figure 7.** H<sub>2</sub>-TPR profiles obtained for Ni-AE/USY catalysts.

### 3.2.2. Reduced Catalysts Characterization

Again, reduced catalysts were characterized by XRD (patterns presented in Figure 5), being clear that the reduction at 470 °C did not induce the formation of metallic nickel over the Ni-Mg/USY catalyst. For this reason, this sample was additionally reduced at 740 °C being then confirmed the presence of Ni<sup>0</sup> phases ( $d_{\text{Ni}^0} = 12$  nm; Dispersion = 8.4%). In the case of Ni-Ca/USY, an average Ni<sup>0</sup> crystallite size of 14 nm (Dispersion = 7.2%) was obtained after reduction at 470 °C. As a result, both Mg (when reducing at higher temperature) and Ca favored the metallic dispersion, as the reference Ni/USY presented Ni<sup>0</sup> crystallites of 18 nm and a dispersion of 5.6%. The decomposition of the CaCO<sub>3</sub> present in the calcined Ni-Ca/USY was attained during the reduction at 470 °C, in agreement with literature [50,51], i.e., CaCO<sub>3</sub> decomposition occurs at lower temperatures in presence of H<sub>2</sub>, especially if Ni, Ru or Rh metals are present, contributing to the formation of CO and/or CH<sub>4</sub>. However, CaO diffraction peaks (32.3, 37.5 and 54.0°) were not observed. Regarding the USY structure preservation, no diffraction peaks attributed to the zeolite were found in Ni-Mg/USY reduced at 740 °C nor Ni-Ca/USY (reduced at 470 °C). However, these peaks could be still found in Ni-Mg/USY sample when performing a reduction treatment at 470 °C, suggesting that for this sample the use of 740 °C was responsible for the collapse of the structure.

### 3.2.3. Catalytic Performances

Regarding the performances exhibited by Ni-AE/USY catalysts under CO<sub>2</sub> methanation conditions after a pre-reduction at 470 °C (Figure 8), results (CO<sub>2</sub> conversion, CH<sub>4</sub> selectivity and CH<sub>4</sub> yield) followed the trend: Ni/USY  $\approx$  Ni-Ca/USY > Ni-Mg/USY. To be pointed out is the similarity between the results exhibited by the monometallic reference (Ni/USY) and the Ni-Ca/USY sample below 350 °C while a difference on the conversion and yield <10% was found in the 350–450 °C temperature range. In the case of Ni-Mg/USY, an additional catalytic test was performed after reduction at 740 °C to allow the formation of Ni<sup>0</sup> phases. Results can be seen in Figure S8, which evidences that, in spite of the beneficial effect of increasing the pre-reduction treatment for reducing the Ni-Mg solid solution, no enhancement of the performances was achieved.

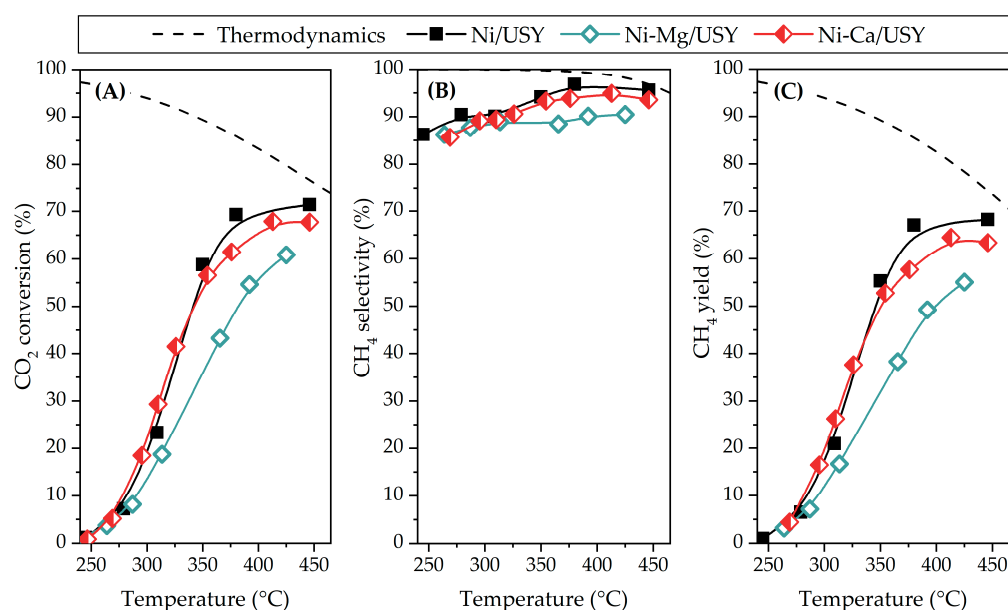


**Figure 8.** Catalytic performances obtained for Ni-AE/USY catalysts after reduction at 470 °C: (A) CO<sub>2</sub> conversion; (B) CH<sub>4</sub> selectivity and (C) CH<sub>4</sub> yield. Operating conditions: 1 bar, 86 100 mL h<sup>-1</sup> g<sub>cat</sub><sup>-1</sup> and CO<sub>2</sub>:H<sub>2</sub>:N<sub>2</sub> = 9:36:10.

### 3.2.4. Spent Catalysts Characterization

XRD patterns of the spent catalysts (Figure S4) revealed that, after tests, no diffraction peaks ascribed to the USY zeolite were found in Ni-Mg/USY (reduced at 470 and 740 °C) nor Ni-Ca/USY, being in the last found diffraction peaks ascribed to CaCO<sub>3</sub> (23.0, 29.4, 36.0, 39.4, 43.1, 47.5, 48.5, 57.4 and 64.6°). This indicates that, during the reaction in presence of CO<sub>2</sub>, calcium carbonate was progressively formed. In addition to this, Ni<sup>0</sup> phases peaks could be clearly found in the Ni-Mg/USY reduced at 740 °C and Ni-Ca/USY catalysts, while the use of a lower reduction temperature for the Mg-containing sample did not allow the complete reduction of the Ni-Mg solid solution during the catalytic test. The low intensity of the Ni<sup>0</sup> peak at ≈44.5° may indicate that the amount of metallic nickel on the sample was low and/or the phases were highly dispersed. Based on the calculation of the average Ni<sup>0</sup> crystallite sizes and comparison with the values obtained after reduction (Figure S5), the occurrence of sintering or metal agglomeration was expected on Ni-Ca/USY catalyst ( $\Delta d_{\text{Ni}^0} = 5 \text{ nm}$ ).

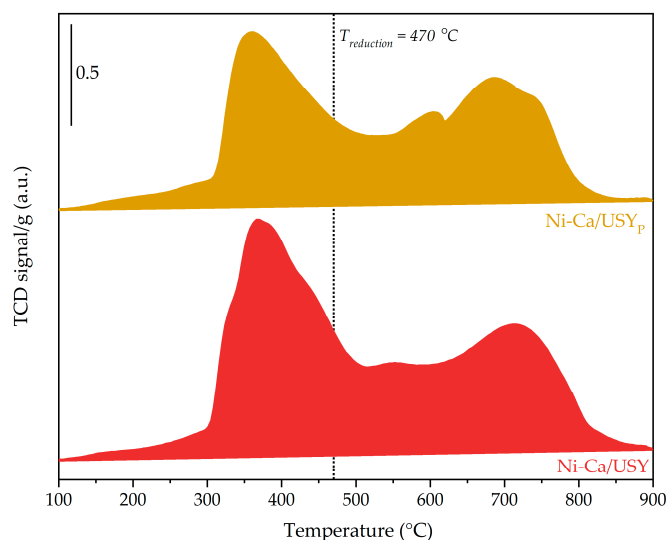
### 3.3. Impregnation Solvent Effect

As a final step, and considering the beneficial effect reported in literature when using 2-propanol instead of distilled water as impregnation solvent in Ni-based zeolites [26], the most outstanding bimetallic catalyst (Ni-Ca/USY) was prepared following the same procedure but replacing the chosen solvent (Ni-Ca/USY<sub>P</sub>). The main properties of these two catalysts are summarized on Table 3, being their N<sub>2</sub> isotherms and XRD patterns presented in Figures S9 and S10, respectively. As seen, their textural properties (Table 3) were similar in terms of V<sub>meso</sub> and S<sub>ext</sub>, while the use of 2-propanol as solvent did not lead to a remarkable decrease in the V<sub>micro</sub>. As already discussed, this reduction on the V<sub>micro</sub> on the Ni-Ca/USY could not be only due to the damage of the zeolite structure, as the diffraction peaks of USY could be still found in the calcined catalyst (Figure S10). Similarly, zeolite diffraction peaks were found in the Ni-Ca/USY<sub>P</sub>. Additionally, in terms of average NiO crystallite sizes (Table 3), the positive effect of 2-propanol on this parameter was confirmed (from 18 to 7 nm when using water or 2-propanol as impregnation solvent, respectively). In terms of interaction with water (h indexes, Table 3), a lower h index was found in Ni-Ca/USY<sub>P</sub>. Furthermore, no remarkable changes in the reducibility of Ni species were observed by H<sub>2</sub>-TPR (Figure 9), being the profiles equivalent.

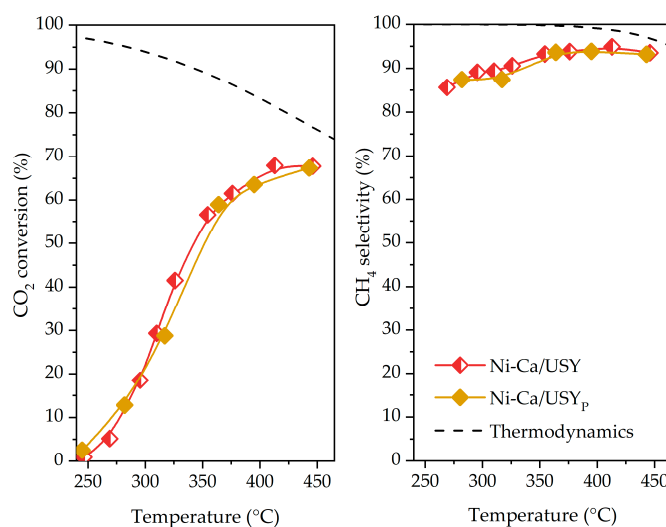
**Table 3.** Main properties obtained for the Ni-Ca/USY and Ni-Ca/USY<sub>P</sub> catalysts after calcination.

Catalyst	V <sub>micro</sub> <sup>1</sup> (cm <sup>3</sup> g <sup>-1</sup> )	V <sub>meso</sub> <sup>2</sup> (cm <sup>3</sup> g <sup>-1</sup> )	S <sub>ext</sub> <sup>1</sup> (m <sup>2</sup> g <sup>-1</sup> )	d <sub>NiO</sub> <sup>3</sup> (nm)	h Index <sup>4</sup>
Ni-Ca/USY	<0.01	0.11	77	18	0.70
Ni-Ca/USY <sub>P</sub>	0.11	0.11	83	7	0.57

<sup>1</sup> Micropores volume and external surface area obtained from *t*-plot method; <sup>2</sup> mesopores volume obtained as V<sub>total</sub>-V<sub>micro</sub>; <sup>3</sup> average NiO crystallite sized determined applying Scherrer equation; <sup>4</sup> hydrophobicity index obtained from TGA analysis of the catalysts saturated with water.

**Figure 9.** H<sub>2</sub>-TPR profiles obtained for Ni-Ca/USY and Ni-Ca/USY<sub>P</sub> catalysts.

In terms of catalytic performances (Figure 10), similar CO<sub>2</sub> conversion and CH<sub>4</sub> selectivity were found for both catalysts, despite the lower Ni<sup>0</sup> crystallites size determined for Ni-Ca/USY<sub>P</sub> (10 nm) when comparing to Ni-Ca/USY (14 nm). Consequently, the effect of the impregnation solvent on the performances of these bimetallic catalysts seems to be negligible. As performed previously, spent samples were characterized by XRD, being the patterns presented in Figure S4 and the average Ni<sup>0</sup> crystallites sizes after reduction and test in Figure S5. As observed, an increase of 4 nm in the Ni<sup>0</sup> crystallite size was found for Ni-Ca/USY<sub>P</sub>, similar to the one of Ni-Ca/USY sample.

**Figure 10.** Catalytic performances obtained for Ni-Ca/USY and Ni-Ca/USY<sub>P</sub> catalysts after reduction at 470 °C. Operating conditions: 1 bar, 86 100 mL h<sup>-1</sup> g<sub>cat</sub><sup>-1</sup> and CO<sub>2</sub>:H<sub>2</sub>:N<sub>2</sub> = 9:36:10.

## 4. Discussion

In this work, the influence of adding alkali and alkali-earth metals in the formulation of Ni-based USY zeolite catalysts for CO<sub>2</sub> methanation was assessed, with the aim of studying the influence of the metal nature in the physicochemical and catalytic properties.

### 4.1. Alkali Metals

Ni-A/USY catalysts containing Li, K or Cs were first synthesized and the analysis of the textural properties (Table 1) was coherent with XRD data. The drastic decrease on the micropores volumes ( $V_{\text{micro}}$ ) together with the disappearance of the characteristic zeolite diffraction peaks (mainly in the  $2\theta$  range of 5–35°) were indicators of the structure collapse. This zeolite destruction could be attributed to the reaction between Li, K and Cs with the Si from the zeolite, being this confirmed in the case of Ni-Li/USY catalyst (Figure 1) and expected for K and Cs-containing samples.

In addition, the presence of NiO and Ni<sup>0</sup> was identified in the samples after calcination and reduction, respectively, in all Ni-A/USY catalysts. However, no enhancement of the Ni<sup>0</sup> dispersion was observed when incorporating alkali metals in the formulation (Ni<sup>0</sup> crystallites larger in Ni-A/USY samples than on the Ni/USY reference). This effect could be related to the destruction of the zeolite porosity ( $V_{\text{meso}}$  significantly reduced with the addition of alkali metals, Table 2), which was found to improve the metallic dispersion through the establishment of proper metal-support interactions and the location of NiO/Ni<sup>0</sup> particles inside the cavities (confinement effect) [22,24].

Besides, and considering the relevance of the interaction of the catalysts with water (product of the reaction with inhibitory effect) and carbon dioxide (reactant), these two properties were analyzed. While the bimetallic systems revealed a lower hydrophobic character (h indexes, Table 2), the interaction of the samples with CO<sub>2</sub> was highly affected by the alkali metal nature (CO<sub>2</sub> uptakes in adsorption–desorption cycles, Figure 2). Even if Ni-K/USY presented a negligible CO<sub>2</sub> adsorption capacity, Ni-Li/USY and Ni-Cs/USY exhibited higher CO<sub>2</sub> uptakes than the Ni/USY reference. The CO<sub>2</sub> adsorption capacity was doubled when incorporating alkali metals (except for K addition) in catalysts' formulation.

Furthermore, and based on the H<sub>2</sub>-TPR profiles analysis (Figure 3), it was concluded that the incorporation of alkali metals induced some modifications on the NiO particles interaction with the support. Overall, K and Cs-containing catalysts exhibited a remarkable NiO reduction degree below the pre-reduction temperature (470 °C), suggesting the establishment of weaker metal-support interactions.

In terms of catalytic performances (Figure 4), none of the bimetallic catalysts exhibited better results than the reference (Ni/USY), which could be ascribed to the zeolite destruction and the absence of improvements in terms of metal-support interactions, hydrophobicity or metallic dispersion. Based in the literature [12], the zeolite support plays a role in the CO<sub>2</sub> methanation reaction as, among all: (i) it can provide additional active sites for CO<sub>2</sub> adsorption; (ii) it can reduce the inhibitory role of water in the reaction; (iii) their cavities and cages can act CO<sub>2</sub> molecules reservoir; or (iv) it can induce a confinement effect of the metal particles inside its pores, especially in cases where the zeolite contains mesopores, which is the case of the USY used in the present study. Consequently, the severe damage observed in the zeolite structure leads to a reduction of its positive impact on the reaction, being this probably contributing to the lower performances exhibited by the bimetallic catalysts. When comparing among them, Ni-Cs/USY and Ni-Li/USY samples presented similar performances, while Ni-K/USY exhibited the lowest CO<sub>2</sub> conversions and selectivity to methane. These results could be easily explained by the lower metal dispersion, weaker metal-support interactions and negligible CO<sub>2</sub> adsorption capacity displayed by Ni-K/USY.

The results obtained were mostly in agreement with literature findings. Petala et al. [18] evaluated the influence of incorporating Li, Na, K and Cs in the formulation of Ru/TiO<sub>2</sub> catalysts prepared by sequential impregnation (alkali metals incorporation prior to Ru addition). Authors verified the following trend in terms of performances toward CO<sub>2</sub>

methanation:  $\text{TiO}_2$  (unpromoted) <  $\text{Li} \approx \text{K} < \text{Cs} < \text{Na}$  and suggested that too low promoter/Ru ratios could lead to an inefficient promotion while too high ratios could lead to a poisoning effect. The beneficial effect of alkali metals incorporation over Ru catalysts was attributed to the favored formation of carbonyl species on Ru sites, key for the methanation mechanism over these catalytic systems [52]. Cimino et al. [19] also studied the influence of Li, Na and K incorporation over 1 wt% Ru/ $\text{Al}_2\text{O}_3$  catalysts prepared by sequential impregnation. Authors found out that only Li, which reacted with alumina forming aluminite spinel phase, led to a positive effect on the catalytic performance. They also observed that incorporating the alkali metals after Ru impregnation led to a coverage of Ru sites, reducing the conversion of  $\text{CO}_2$  and promoting CO formation.

Liang et al. [53] evaluated the influence of Na, Mg, K, Ca, Sc, Ti, V, Cr, Mn, Fe, Co, Cu, Zn, Zr, La and Ce incorporation over  $\text{Al}_2\text{O}_3$  followed by Ni addition (sequential impregnation). Among them, Na and K strongly affected the textural properties of the catalysts and the second led to a significantly lower activity and the promotion of CO formation. This behavior was attributed to the improvement of  $\text{H}_2\text{CO}^*$  species formation. In a similar study, Zhang et al. [13] studied the incorporation of K and Na in Co/ $\text{Al}_2\text{O}_3$  catalysts formulation. Authors observed that Na and K reacted with the support and induced  $\text{Al}(\text{OH})_3$  and/or  $\text{NaAlO}_2$  species formation, drastically reducing catalysts' textural properties. In addition, these metals enhanced the affinity to  $\text{HCOO}^*$  and  $\text{CO}_3^{2-}$  species, hindering its successive reduction to  $\text{CH}_4$ , lowering the catalytic performance and favoring coke formation/deposition. Authors did not observe a correlation between the  $\text{CO}_2$  adsorption capacity and the catalytic behavior, with the increase in the basicity induced by Na and K incorporation responsible for a promotion of CO formation.

The higher activity of K-containing catalysts toward RWGS rather than  $\text{CO}_2$  methanation was also reported by other authors in literature [54–56], being related with the difficulties in formate species hydrogenation and/or the easy desorption of CO intermediates from these catalysts, hindering  $\text{CH}_4$  formation. Consequently, based on literature, the lack of enhancements observed in Ni-A/USY catalysts could be related, among all, to: (i) the interaction of alkali metals with the zeolite, damaging its structure and reducing the textural properties; (ii) the strong interaction between some expected intermediates (e.g., carbonates, formates [57]) and the alkali compounds, hindering its further hydrogenation and promoting CO desorption; (iii) the lack of enhancements in terms of metal-support interactions and  $\text{Ni}^0$  metallic dispersion in bimetallic samples; (iv) an inefficient promoter/Ni ratio.

#### 4.2. Alkali-Earth Metals

In terms of Ni-AE/USY catalysts, the incorporation of Mg and Ca was analyzed. Contrary to what found for Ni-A/USY samples, alkali-earth metals did not lead to such a destruction on the zeolite structure (textural properties in Table 2; XRD patterns in Figure 5). This indicated a lower interaction between the metals and the zeolite structure. In addition, while Ni-Mg mixed oxides were formed in the Ni-Mg/USY catalyst (XRD patterns, Figure 5) and their reduction was only completed above 850 °C ( $\text{H}_2$ -TPR profile, Figure 7), Ni-Ca/USY presented the characteristic diffraction peaks of  $\text{CaCO}_3$  phases after calcination while the reduction was expectedly inducing the formation of highly dispersed CaO particles (Figure 5). The strong interaction between Mg and Ni was reported in the literature for zeolite-supported catalysts [46], and motivated carrying out a pre-reduction treatment at a higher temperature (740 °C) for allowing a greater presence of  $\text{Ni}^0$  phases in the catalyst, as confirmed by its XRD pattern presented in Figure 5. In addition, the formation of  $\text{CaCO}_3$  in the calcined Ni-Ca/USY sample could be explained by the contact of the sample with the atmosphere after calcination. Regarding catalyst interaction with water (h indexes, Table 2) and carbon dioxide ( $\text{CO}_2$  uptakes in adsorption–desorption cycles, Figure 6), Ni-Ca/USY revealed a higher  $\text{CO}_2$  adsorption–desorption stability over the time and a more hydrophobic character. In addition, and as found for alkali metals incorpo-

ration, bimetallic catalysts containing Mg and Ca presented CO<sub>2</sub> adsorption capacities considerably higher (more than double) than the monometallic Ni/USY.

In terms of catalytic performances (Figure 8), the incorporation of Ca led to better results, with Ni-Mg/USY exhibiting lower CH<sub>4</sub> yields, including after a pre-reduction treatment at 740 °C (Figure S8). The better results exhibited by Ni-Ca/USY rather than Ni-Mg/USY could be attributed to the more favorable reducibility of Ni species over the first catalyst as well as to its higher hydrophobic character. In addition, the negative impact of using a higher pre-reduction temperature in the performances of Ni-Mg/USY could be ascribed to the damage of the zeolite structure (zeolite diffraction peaks not found in this sample, Figure 5), reducing the positive impact of the zeolite structure/porosity on the results.

When comparing the results of the alkali and alkali-earth metals-containing catalysts, the preservation of the zeolite structure in the Ni-AE/USY samples and the slightly higher metallic dispersion achieved with this series could be in the origin of the higher performances exhibited by these catalysts. This tendency was also verified by Zhang et al. [13] when incorporating Mg and Ca in Co/Al<sub>2</sub>O<sub>3</sub> catalysts. Authors observed that the less negative impact of alkali-earth metals on the performances when comparing with Na and K was due to the inhibition of sintering processes in Co particles in presence of Mg and Ca. However, this tendency was not found in this work. When analyzing Ni<sup>0</sup> crystallite sizes after reduction and catalytic tests (Figure S4), it was observed that Li and Ca-containing catalysts were those presenting a more significant enlargement of nickel particles. In addition, Liang et al. [53] also reported that, even if the incorporation of Mg and Ca to Ni/Al<sub>2</sub>O<sub>3</sub> catalysts improved the basicity, no positive effects were found in the catalytic performances.

Furthermore, Guo et al. [20] and Liang et al. [15] obtained similar results for Ni/SiO<sub>2</sub> and Ni/Al<sub>2</sub>O<sub>3</sub> catalysts, respectively, promoted with Mg and Ca (sequentially impregnated; Ni added in the second stage). The formation of stable carbonate species over MgO and CaO was suggested to play a negative effect in the reaction mechanism. In our work, the presence of CaCO<sub>3</sub> in the spent Ni-Ca/USY catalyst was detected (Figure S4) and it could be in the origin of the lower performances exhibited by this catalyst when compared to the Ni/USY at higher reaction temperatures (350–450 °C). Thus, the formation of these species during the catalytic test could be responsible for a reduction in the available CaO sites able to adsorb and/or activate CO<sub>2</sub> molecules.

Regarding the use of 2-propanol instead of water as impregnation solvent, responsible for an enhancement of the metallic dispersion in previous studies dealing with Ni/USY zeolites [26], no remarkable differences in terms of catalytic performances were found for Ni-Ca/USY catalysts (Figure 10). While the use of 2-propanol improved the metallic dispersion and textural properties (Table 3), the lack of enhancements in terms of metal-support interactions (H<sub>2</sub>-TPR profiles, Figure 9) and the reduction of the hydrophobicity (h indexes, Table 3) could explain the obtained results.

#### 4.3. Future Perspectives

Overall, both in the alkali and alkali-earth metals series, the destruction/damage of the zeolite structure used as support (USY with global Si/Al of ≈38), was responsible for a negative impact on the properties and performances of the synthesized catalysts. In this way, and despite the well-known hydrothermal stability of USY zeolites, the high Si/Al ratio of the chosen support, achieved commercially by consecutive dealumination steps and responsible for the creation of holes/cavities acting as mesopores, could be responsible for a lower structural resistance of the material. Consequently, the utilization of a more common USY zeolite (with a lower Si/Al ratio of 2–5) could represent a promising strategy for future studies. In addition, and considering the findings reported on literature regarding the relevance of the promoter/active metal ratio and the preparation method strategy, evaluating the impacts of using lower promoter/Ni ratios or preparing sequen-

tially impregnated samples could be valuable. Finally, the incorporation of other alkali and alkali-earth metals such as sodium and barium could be focus of study.

## 5. Conclusions

In this work, the influence of incorporating alkali (Li, K and Cs) and alkali-earth (Mg and Ca) metals over Ni/USY zeolite catalysts applied in CO<sub>2</sub> methanation reaction was analyzed. The addition of alkali metals led to a remarkable decrease in the catalytic performances as, based on the analysis of their structural and textural properties, the introduction of Li, K and Cs induced a severe destruction of the zeolite structure. In addition, regarding Mg and Ca incorporation, even if a lower impact in the zeolite structure was observed, the formation of Ni-Mg solid solution (Ni-Mg/USY) and the formation of stable CaCO<sub>3</sub> during the reaction (Ni-Ca/USY) were suggested as responsible for the lack of improvements in the performances.

Overall, in spite of the enhancement of the CO<sub>2</sub> adsorption capacity when adding alkali (Li and Cs) and alkali-earth (Mg and Ca) metals to Ni/USY catalysts, no remarkable enhancement of the performances was observed. Among them, Ca was found as the most interesting metal, which was ascribed to the slight improvement of the Ni<sup>0</sup> dispersion.

**Supplementary Materials:** The following are available online at <https://www.mdpi.com/article/10.3390/pr9101846/s1>, Figure S1: N<sub>2</sub> isotherms obtained for the Ni-A/USY catalysts after calcination; Figure S2: TGA results for Ni-A/USY and Ni-AE/USY catalysts after saturation with water; Figure S3: DRS UV-Vis spectra obtained for the Ni-A/USY catalysts after calcination; Figure S4: XRD patterns collected for all the catalysts from this work after catalytic tests; Figure S5: Ni<sup>0</sup> crystallite sizes determined from XRD data and using Scherrer equation for all the catalysts from this work after reduction and catalytic tests; Figure S6: N<sub>2</sub> isotherms obtained for the Ni-AE/USY catalysts after calcination; Figure S7: DRS UV-Vis spectra obtained for the Ni-AE/USY catalysts after calcination; Figure S8: Effect of the pre-reduction temperature in the CO<sub>2</sub> conversion and CH<sub>4</sub> selectivity of Ni-Mg/USY catalyst. Operating conditions: 1 bar, 86 100 mL h<sup>-1</sup> g<sub>cat</sub><sup>-1</sup>, CO<sub>2</sub>:H<sub>2</sub>:N<sub>2</sub> = 9:36:10; Figure S9: N<sub>2</sub> isotherms obtained for the Ni-Ca/USY and Ni-Ca/USY<sub>P</sub> catalysts after calcination; Figure S10: XRD patterns obtained for the Ni-Ca/USY and Ni-Ca/USY<sub>P</sub> catalysts after calcination and reduction.

**Author Contributions:** Conceptualization, M.C.B.; methodology, C.G., M.C.B. and P.T.; experimental data curation, C.G., M.C.B. and P.T.; writing—original draft preparation, M.C.B.; writing—review and editing, P.T., J.M.L. and C.H.; supervision, M.C.B., J.M.L. and C.H. All authors have read and agreed to the published version of the manuscript.

**Funding:** This research was funded by Fundação para a Ciência e Tecnologia (FCT), through projects UIDB/00100/2020 and UIDP/00100/2020.

**Institutional Review Board Statement:** Not applicable.

**Informed Consent Statement:** Not applicable.

**Data Availability Statement:** All data are reported in the paper.

**Conflicts of Interest:** The authors declare no conflict of interest.

## References

1. Blanco, H.; Faaij, A. A Review at the Role of Storage in Energy Systems with a Focus on Power to Gas and Long-Term Storage. *Renew. Sustain. Energy Rev.* **2018**, *81*, 1049–1086. [[CrossRef](#)]
2. Thema, M.; Bauer, F.; Sterner, M. Power-to-Gas: Electrolysis and Methanation Status Review. *Renew. Sustain. Energy Rev.* **2019**, *112*, 775–787. [[CrossRef](#)]
3. Jin Lee, W.; Li, C.; Prajitno, H.; Yoo, J.; Patel, J.; Yang, Y.; Lim, S. Recent Trend in Thermal Catalytic Low Temperature CO<sub>2</sub> Methanation: A Critical Review. *Catal. Today* **2020**, *368*, 2–19. [[CrossRef](#)]
4. Rönsch, S.; Schneider, J.; Matthischke, S.; Schlüter, M.; Götz, M.; Lefebvre, J.; Prabhakaran, P.; Bajohr, S. Review on Methanation—From Fundamentals to Current Projects. *Fuel* **2016**, *166*, 276–296. [[CrossRef](#)]
5. Malara, A.; Frontera, P.; Antonucci, P.; Macario, A. Smart Recycling of Carbon Oxides: Current Status of Methanation Reaction. *Curr. Opin. Green Sustain. Chem.* **2020**, *26*, 100376. [[CrossRef](#)]

6. Ashok, J.; Pati, S.; Hongmanorom, P.; Tianxi, Z.; Junmei, C.; Kawi, S. A Review of Recent Catalyst Advances in CO<sub>2</sub> Methanation Processes. *Catal. Today* **2020**, *356*, 471–489. [CrossRef]
7. Huynh, H.L.; Yu, Z. CO<sub>2</sub> Methanation on Hydrotalcite-Derived Catalysts and Structured Reactors: A Review. *Energy Technol.* **2020**, *8*, 1901475. [CrossRef]
8. Lv, C.; Xu, L.; Chen, M.; Cui, Y.; Wen, X.; Li, Y.; Wu, C.; Yang, B.; Miao, Z.; Hu, X.; et al. Recent Progresses in Constructing the Highly Efficient Ni Based Catalysts With Advanced Low-Temperature Activity Toward CO<sub>2</sub> Methanation. *Front. Chem.* **2020**, *8*, 269. [CrossRef] [PubMed]
9. Erdőhelyi, A. Hydrogenation of Carbon Dioxide on Supported Rh Catalysts. *Catalysts* **2020**, *10*, 155. [CrossRef]
10. Bacariza, M.C.; Spataru, D.; Karam, L.; Lopes, J.M.; Henriques, C. Promising Catalytic Systems for CO<sub>2</sub> Hydrogenation into CH<sub>4</sub>: A Review of Recent Studies. *Processes* **2020**, *8*, 1646. [CrossRef]
11. Gao, J.; Liu, Q.; Gu, F.; Liu, B.; Zhong, Z.; Su, F. Recent Advances in Methanation Catalysts for the Production of Synthetic Natural Gas. *RCS Adv.* **2015**, *5*, 22759–22776. [CrossRef]
12. Bacariza, M.C.; Graça, I.; Lopes, J.M.; Henriques, C. Tuning Zeolite Properties towards CO<sub>2</sub> Methanation: An Overview. *ChemCatChem* **2019**, *11*, 2388–2400. [CrossRef]
13. Zhang, Z.; Zhang, X.; Zhang, L.; Gao, J.; Shao, Y.; Dong, D.; Zhang, S.; Liu, Q.; Xu, L.; Hu, X. Impacts of Alkali or Alkaline Earth Metals Addition on Reaction Intermediates Formed in Methanation of CO<sub>2</sub> over Cobalt Catalysts. *J. Energy Inst.* **2020**, *93*, 1581–1596. [CrossRef]
14. Wang, S.; Yan, S.; Ma, X.; Gong, J. Recent Advances in Capture of Carbon Dioxide Using Alkali-Metal-Based Oxides. *Energy Environ. Sci.* **2011**, *4*, 3805–3819. [CrossRef]
15. Liang, C.; Hu, X.; Wei, T.; Jia, P.; Zhang, Z.; Dong, D.; Zhang, S.; Liu, Q.; Hu, G. Methanation of CO<sub>2</sub> over Ni/Al<sub>2</sub>O<sub>3</sub> Modified with Alkaline Earth Metals: Impacts of Oxygen Vacancies on Catalytic Activity. *Int. J. Hydrog. Energy* **2019**, *44*, 8197–8213. [CrossRef]
16. Liu, K.; Xu, X.; Xu, J.; Fang, X.; Liu, L.; Wang, X. The Distributions of Alkaline Earth Metal Oxides and Their Promotional Effects on Ni/CeO<sub>2</sub> for CO<sub>2</sub> Methanation. *J. Co<sub>2</sub> Util.* **2020**, *38*, 113–124. [CrossRef]
17. Méndez-Mateos, D.; Barrio, V.L.; Requies, J.M.; Cambra, J.F. Effect of the Addition of Alkaline Earth and Lanthanide Metals for the Modification of the Alumina Support in Ni and Ru Catalysts in CO<sub>2</sub> Methanation. *Catalysts* **2021**, *11*, 353. [CrossRef]
18. Petala, A.; Panagiotopoulou, P. Methanation of CO<sub>2</sub> over Alkali-Promoted Ru/TiO<sub>2</sub> Catalysts: I. Effect of Alkali Additives on Catalytic Activity and Selectivity. *Appl. Catal. B Environ.* **2018**, *224*, 919–927. [CrossRef]
19. Cimino, S.; Boccia, F.; Lisi, L. Effect of Alkali Promoters (Li, Na, K) on the Performance of Ru/Al<sub>2</sub>O<sub>3</sub> Catalysts for CO<sub>2</sub> Capture and Hydrogenation to Methane. *J. Co<sub>2</sub> Util.* **2020**, *37*, 195–203. [CrossRef]
20. Guo, M.; Lu, G. The Difference of Roles of Alkaline-Earth Metal Oxides on Silica-Supported Nickel Catalysts for CO<sub>2</sub> Methanation. *RSC Adv.* **2014**, *4*, 58171–58177. [CrossRef]
21. Tsiotsias, A.I.; Charisiou, N.D.; Yentekakis, I.V.; Goula, M.A. The Role of Alkali and Alkaline Earth Metals in the CO<sub>2</sub> Methanation Reaction and the Combined Capture and Methanation of CO<sub>2</sub>. *Catalysts* **2020**, *10*, 812. [CrossRef]
22. Bacariza, M.C.; Graça, I.; Lopes, J.M.; Henriques, C. Enhanced Activity of CO<sub>2</sub> Hydrogenation to CH<sub>4</sub> over Ni Based Zeolites through the Optimization of the Si/Al Ratio. *Microporous Mesoporous Mater.* **2018**, *267*, 9–19. [CrossRef]
23. Bacariza, M.C.; Bértolo, R.; Graça, I.; Lopes, J.M.; Henriques, C. The Effect of the Compensating Cation on the Catalytic Performances of Ni/USY Zeolites towards CO<sub>2</sub> Methanation. *J. Co<sub>2</sub> Util.* **2017**, *21*, 280–291. [CrossRef]
24. Bacariza, M.C.; Maleval, M.; Graça, I.; Lopes, J.M.; Henriques, C. Power-to-Methane over Ni/Zeolites: Influence of the Framework Type. *Microporous Mesoporous Mater.* **2019**, *274*, 102–112. [CrossRef]
25. Bacariza, M.C.; Graça, I.; Lopes, J.M.; Henriques, C. Ni-Ce/Zeolites for CO<sub>2</sub> Hydrogenation to CH<sub>4</sub>: Effect of the Metal Incorporation Order. *ChemCatChem* **2018**, *10*, 2773–2781. [CrossRef]
26. Bacariza, M.C.; Amjad, S.; Teixeira, P.; Lopes, J.M.; Henriques, C. Boosting Ni Dispersion on Zeolite-Supported Catalysts for CO<sub>2</sub> Methanation: The Influence of the Impregnation Solvent. *Energy Fuels* **2020**, *34*, 14656–14666. [CrossRef]
27. Luisetto, I.; Tuti, S.; Romano, C.; Boaro, M.; Di Bartolomeo, E.; Kesavan, J.K.; Kumar, S.S.; Selvakumar, K. Dry Reforming of Methane over Ni Supported on Doped CeO<sub>2</sub>: New Insight on the Role of Dopants for CO<sub>2</sub> Activation. *J. Co<sub>2</sub> Util.* **2019**, *30*, 63–78. [CrossRef]
28. Chayed, N.F.; Badar, N.; Rusdi, R.; Kamarudin, N.; Kamarulzaman, N. Optical Band Gap Energies of Magnesium Oxide (MgO) Thin Film and Spherical Nanostructures. *AIP Conf. Proc.* **2011**, *1400*, 328–332. [CrossRef]
29. Nemade, K.R.; Waghuley, S.A. Synthesis of MgO Nanoparticles by Solvent Mixed Spray Pyrolysis Technique for Optical Investigation. Available online: <https://www.hindawi.com/journals/ijmet/2014/389416/> (accessed on 5 February 2018).
30. Palacio, L.A.; Silva, E.R.; Catalão, R.; Silva, J.M.; Hoyos, D.A.; Ribeiro, F.R.; Ribeiro, M.F. Performance of Supported Catalysts Based on a New Copper Vanadate-Type Precursor for Catalytic Oxidation of Toluene. *J. Hazard. Mater.* **2008**, *153*, 628–634. [CrossRef]
31. Bacariza, M.C.; Graça, I.; Westermann, A.; Ribeiro, M.F.; Lopes, J.M.; Henriques, C. CO<sub>2</sub> Hydrogenation Over Ni-Based Zeolites: Effect of Catalysts Preparation and Pre-Reduction Conditions on Methanation Performance. *Top. Catal.* **2015**, *59*, 314–325. [CrossRef]
32. Graça, I.; González, L.V.; Bacariza, M.C.; Fernandes, A.; Henriques, C.; Lopes, J.M.; Ribeiro, M.F. CO<sub>2</sub> Hydrogenation into CH<sub>4</sub> on NiHNaUSY Zeolites. *Appl. Catal. B Environ.* **2014**, *147*, 101–110. [CrossRef]

33. Treacy, M.M.; Higgins, J.B. *Collection of Simulated XRD Powder Patterns for Zeolites*; Elsevier: Amsterdam, The Netherlands, 2007; ISBN 978-0-444-53067-7.
34. Zhang, Y.; Gao, Y.; Louis, B.; Wang, Q.; Lin, W. Fabrication of Lithium Silicates from Zeolite for CO<sub>2</sub> Capture at High Temperatures. *J. Energy Chem.* **2019**, *33*, 81–89. [[CrossRef](#)]
35. Grasso, M.L.; Arneodo Larochette, P.; Gennari, F.C. CO<sub>2</sub> Capture Properties of Li<sub>4</sub>SiO<sub>4</sub> after Aging in Air at Room Temperature. *J. Co<sub>2</sub> Util.* **2020**, *38*, 232–240. [[CrossRef](#)]
36. Hubble, R.A.; Lim, J.Y.; Dennis, J.S. Kinetic Studies of CO<sub>2</sub> Methanation over a Ni/γ-Al<sub>2</sub>O<sub>3</sub> Catalyst. *Faraday Discuss.* **2016**, *192*, 529–544. [[CrossRef](#)] [[PubMed](#)]
37. Li, S.; Huang, H.; Yang, X.; Bai, Y.; Li, J.; Kobayashi, N.; Kubota, M. Hydrophilic Substance Assisted Low Temperature LiOH·H<sub>2</sub>O Based Composite Thermochemical Materials for Thermal Energy Storage. *Appl. Therm. Eng.* **2018**, *128*, 706–711. [[CrossRef](#)]
38. Olivares-Marín, M.; Drage, T.C.; Maroto-Valer, M.M. Novel Lithium-Based Sorbents from Fly Ashes for CO<sub>2</sub> Capture at High Temperatures. *Int. J. Greenh. Gas. Control.* **2010**, *4*, 623–629. [[CrossRef](#)]
39. Beyer, H.; Meini, S.; Tsiouvaras, N.; Piana, M.; Gasteiger, H.A. Thermal and Electrochemical Decomposition of Lithium Peroxide in Non-Catalyzed Carbon Cathodes for Li–Air Batteries. *Phys. Chem. Chem. Phys.* **2013**, *15*, 11025–11037. [[CrossRef](#)] [[PubMed](#)]
40. Zhang, G.; Peng, Z.; Li, C. A Study of Thermal Behavior of Cesium Phosphate. *J. Anal. Calorim.* **2016**, *124*, 1063–1070. [[CrossRef](#)]
41. Fleger, Y.; Rosenbluh, M. Surface Plasmons and Surface Enhanced Raman Spectra of Aggregated and Alloyed Gold-Silver Nanoparticles. *Int. J. Opt.* **2009**. [[CrossRef](#)]
42. Mohammadjoo, M.; Naderi Khorshidi, Z.; Sadreznhaad, S.K.; Mazinani, V. Synthesis and Characterization of Nickel Oxide Nanoparticle with Wide Band Gap Energy Prepared via Thermochemical Processing. *IJNN* **2014**, *4*, 6–9.
43. Ning, X.; Lu, Y.; Fu, H.; Wan, H.; Xu, Z.; Zheng, S. Template Mediated Ni(II) Dispersion in Mesoporous SiO<sub>2</sub> for Preparation of Highly Dispersed Ni Catalysts: Influence of Template Type. *ACS Appl. Mater. Interfaces* **2017**. [[CrossRef](#)] [[PubMed](#)]
44. Ruckenstein, E.; Hang Hu, Y. Methane Partial Oxidation over NiO/MgO Solid Solution Catalysts. *Appl. Catal. A Gen.* **1999**, *183*, 85–92. [[CrossRef](#)]
45. Guo, M.; Lu, G. The Effect of Impregnation Strategy on Structural Characters and CO<sub>2</sub> Methanation Properties over MgO Modified Ni/SiO<sub>2</sub> Catalysts. *Catal. Commun.* **2014**, *54*, 55–60. [[CrossRef](#)]
46. Bacariza, M.C.; Graça, I.; Bebiano, S.S.; Lopes, J.M.; Henriques, C. Magnesium as Promoter of CO<sub>2</sub> Methanation on Ni-Based USY Zeolites. *Energy Fuels* **2017**, *31*, 9776–9789. [[CrossRef](#)]
47. Teixeira, P.; Mohamed, I.; Fernandes, A.; Silva, J.; Ribeiro, F.; Pinheiro, C.I.C. Enhancement of Sintering Resistance of CaO-Based Sorbents Using Industrial Waste Resources for Ca-Looping in the Cement Industry. *Sep. Purif. Technol.* **2020**, *235*, 116190. [[CrossRef](#)]
48. Teixeira, P.; Hipólito, J.; Fernandes, A.; Ribeiro, F.; Pinheiro, C.I.C. Tailoring Synthetic Sol–Gel CaO Sorbents with High Reactivity or High Stability for Ca-Looping CO<sub>2</sub> Capture. *Ind. Eng. Chem. Res.* **2019**, *58*, 8484–8494. [[CrossRef](#)]
49. Kong, M.; Yang, Q.; Fei, J.; Zheng, X. Experimental Study of Ni/MgO Catalyst in Carbon Dioxide Reforming of Toluene, a Model Compound of Tar from Biomass Gasification. *Int. J. Hydrog. Energy* **2012**, *37*, 13355–13364. [[CrossRef](#)]
50. Belete, T.T.; van de Sanden, M.C.M.; Gleeson, M.A. Effects of Transition Metal Dopants on the Calcination of CaCO<sub>3</sub> under Ar, H<sub>2</sub>O and H<sub>2</sub>. *J. Co<sub>2</sub> Util.* **2019**, *31*, 152–166. [[CrossRef](#)]
51. Padeste, C.; Reller, A.; Oswald, H.R. The Influence of Transition Metals on the Thermal Decomposition of Calcium Carbonate in Hydrogen. *Mater. Res. Bull.* **1990**, *25*, 1299–1305. [[CrossRef](#)]
52. Panagiotopoulou, P. Methanation of CO<sub>2</sub> over Alkali-Promoted Ru/TiO<sub>2</sub> Catalysts: II. Effect of Alkali Additives on the Reaction Pathway. *Appl. Catal. B Environ.* **2018**, *236*, 162–170. [[CrossRef](#)]
53. Liang, C.; Ye, Z.; Dong, D.; Zhang, S.; Liu, Q.; Chen, G.; Li, C.; Wang, Y.; Hu, X. Methanation of CO<sub>2</sub>: Impacts of Modifying Nickel Catalysts with Variable-Valence Additives on Reaction Mechanism. *Fuel* **2019**, *254*, 115654. [[CrossRef](#)]
54. Büchel, R.; Baiker, A.; Pratsinis, S.E. Effect of Ba and K Addition and Controlled Spatial Deposition of Rh in Rh/Al<sub>2</sub>O<sub>3</sub> Catalysts for CO<sub>2</sub> Hydrogenation. *Appl. Catal. A Gen.* **2014**, *477*, 93–101. [[CrossRef](#)]
55. Iloy, R.A.; Jalama, K. Effect of Operating Temperature, Pressure and Potassium Loading on the Performance of Silica-Supported Cobalt Catalyst in CO<sub>2</sub> Hydrogenation to Hydrocarbon Fuel. *Catalysts* **2019**, *9*, 807. [[CrossRef](#)]
56. Zhang, Z.; Hu, X.; Wang, Y.; Hu, S.; Xiang, J.; Li, C.; Chen, G.; Liu, Q.; Wei, T.; Dong, D. Regulation the Reaction Intermediates in Methanation Reactions via Modification of Nickel Catalysts with Strong Base. *Fuel* **2019**, *237*, 566–579. [[CrossRef](#)]
57. Westermann, A.; Azambre, B.; Bacariza, M.C.; Graça, I.; Ribeiro, M.F.; Lopes, J.M.; Henriques, C. Insight into CO<sub>2</sub> Methanation Mechanism over NiUSY Zeolites: An Operando IR Study. *Appl. Catal. B Environ.* **2015**, *174–175*, 120–125. [[CrossRef](#)]